

Spatio-temporal coherent control of atomic systems: weak to strong field transition and breaking of symmetry in 2D maps

This article has been downloaded from IOPscience. Please scroll down to see the full text article.

2008 J. Phys. B: At. Mol. Opt. Phys. 41 074008

(<http://iopscience.iop.org/0953-4075/41/7/074008>)

The Table of Contents and more related content is available

Download details:

IP Address: 132.77.4.129

The article was downloaded on 16/10/2008 at 10:02

Please note that terms and conditions apply.

Spatio-temporal coherent control of atomic systems: weak to strong field transition and breaking of symmetry in 2D maps

H Suchowski, A Natan, B D Bruner and Y Silberberg

Physics of Complex Systems, The Weizmann Institute of Science, Rehovot, Israel

E-mail: haim.suchowski@weizmann.ac.il

Received 8 October 2007, in final form 20 November 2007

Published 25 March 2008

Online at stacks.iop.org/JPhysB/41/074008

Abstract

Coherent control of resonant and non-resonant two-photon absorption processes was examined using a spatio-temporal pulse-shaping technique. By utilizing a combination of temporal focusing and femtosecond pulse-shaping techniques, we spatially control multiphoton absorption processes in a completely deterministic manner. Distinctive symmetry properties emerge through two-dimensional mapping of spatio-temporal data. These symmetries break down in the transition to strong fields, revealing details of strong-field effects such as power broadenings and dynamic Stark shifts. We also present demonstrations of chirp-dependent population transfer in atomic rubidium, as well as the spatial separation of resonant and non-resonant excitation pathways in atomic caesium.

(Some figures in this article are in colour only in the electronic version)

1. Introduction

Coherent control of a quantum system enables an initial quantum state to be steered to a desired final state. Such control schemes have been extensively studied for weak and strong field excitation processes such as population transfer, photodissociation, isomerization control of molecules and molecular alignment [1–3]. By tailoring the spectrum and phase of the exciting laser fields, one can select a specific target state by inducing constructive phase interference between the pathways leading to that target state. Progress in this field has been strongly linked to the emergence of laser technologies needed for performing such experiments, and in this regard, the development and refinement of femtosecond pulse-shaping techniques has been crucial [4–6]. Both analytic (open loop) and adaptive (closed loop) pulse-shaping schemes have been developed, driven by the need to control systems of various complexities. Whereas adaptive techniques employ genetic algorithms that search prohibitively large parameter spaces [7, 8], analytic schemes identify a small number of parameters that drive the physics of interest, based on

knowledge of the system Hamiltonian. The goal of our current research is to place more emphasis on the underlying physics and the development of new analytic control techniques.

Temporal manipulation of multiphoton absorption has received considerable attention in recent years. For weak fields, it was shown that two-photon absorption (TPA) between two levels can be varied continuously between 0 and 100% by varying only the spectral phase of a femtosecond excitation pulse [9, 10]. Control schemes involving three or more energy levels include the study of resonant two-photon absorption [11], the use of chirped excitation pulses [12, 13] and the control of resonant and off-resonant Raman transitions [14]. In these cases, it is necessary to account for the competing effects of nonresonant and resonant excitations and the quantum interferences that may occur between them. Distinguishing these effects and quantifying the contributions of all the competing excitation pathways is an ongoing experimental challenge in the field.

These nominally weak field control techniques are generally not applicable in the strong-field regime. In the

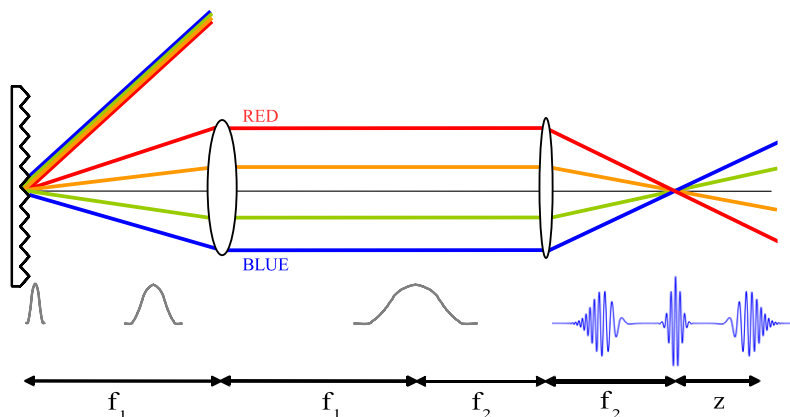


Figure 1. Realization of temporal focusing set-up. This system introduces an optical linear chirp, which is linearly dependent on the position along the optical axis.

weak-field regime, transition rates can be analysed using quantum-mechanical perturbation theory, whereas in the strong-field regime, this type of analysis is no longer valid. Weak field control depends sensitively on the phase relations between interfering transition pathways. In strong fields, transition frequencies are affected by the dynamic Stark shift, and power broadening alters the linewidths of the levels [15, 16]. These effects contribute to the deterioration of the spectral selectivity that is essential for weak field control. Many techniques have emerged to address these issues [17–21], and these persistent challenges are but one reason why strong field control is relatively unexplored.

This paper focuses on the coherent control of two- and three-level atomic systems and how the spatio-temporal control technique can be used to extract information that is difficult, or impractical to measure using purely temporal methods. In particular, the progression between the weak field (perturbative) and strong field (non-perturbative) regimes was considered. Section 2 outlines the design of our spatio-temporal system. Section 3 addresses the analysis of spatio-temporal data and some theoretical background for the experiments reported in this paper. It is shown that distinctive symmetry properties emerge through two-dimensional mapping of spatio-temporal data. The experiments and their results are reported in sections 4 and 5. The transition from weak-to-strong field control in two-level caesium is examined. Strong field effects such as Stark shifts, power broadenings and intensity-dependent enhancements of multiphoton absorption signals can be related to the breaking of the aforementioned symmetries in spatio-temporal diagrams. The problem of distinguishing resonant and nonresonant excitation processes is addressed, and we demonstrate spatial separation of these signals for caesium. In addition, we consider adiabatic population transfer in a three-level system (atomic rubidium), in which the methods of stimulated Raman adiabatic passage (STIRAP) [22] are shown to be fully compatible with spatio-temporal techniques.

2. Experimental design—spatio-temporal control method

The basis of the spatio-temporal control method, compared to purely temporal schemes, is the utilization of temporal focusing. This provides a second degree of freedom in the phase space of shaped pulses. Consider the analogy between spatial focusing and temporal focusing. There is a correspondence between the time variable in the dispersion equations and the transverse space variable in the diffraction equations. That is, the temporal broadening of a pulse due to dispersion is analogous to the spreading of a Gaussian beam due to diffraction. Figure 1 illustrates a system in which dispersion results from geometric origin. It resembles the compressor configuration that was analysed by Martinez [23], except that the second grating is removed. Following the second lens, the pulse acquires positive quadratic phase as it propagates. The net accumulated Group Velocity Dispersion (GVD) of the entire apparatus is zero only at the spatial focus of the second lens f_2 . If the first lens is a cylindrical lens in the horizontal axis, a spatial focus is added in the vertical direction in addition to the described temporal one. The exact relation between the linear chirp and the position on the optical axis is given by the following equation:

$$\frac{d^2\varphi(\Omega)}{d\Omega^2} = -\frac{\omega_l}{c} \left(\frac{d\alpha}{d\Omega}\right)^2 M^2 z = -2\beta z. \quad (1)$$

Here, φ is the total spectral phase, $\frac{d\alpha}{d\Omega}$ is the angular dispersion of the grating, z is the distance measured from the back spatial focal plane of the telescope, ω_l is the centre spectral frequency and $\Omega \equiv \omega - \omega_l$. We have defined the GVD coefficient $\beta \equiv -\frac{\omega_l}{2c} \left(\frac{d\alpha}{d\Omega}\right)^2 M^2$. By convention, the geometric chirp vanishes at the back focal plane of f_2 , where $z = 0$.

Temporal focusing has proved useful in multiphoton microscopy. In standard multiphoton microscopy, a tightly focused beam is scanned in the focal plane of the sample. For each pixel of the image, the two- or three-photon fluorescence signal is measured at a point in the sample, and the full, pixel-by-pixel image is constructed by scanning the excitation

beam over the entire focal plane in the sample. Signal is generated only in the focal plane because of the I^2 or I^3 dependence of the strongly focused beam. The beam's spatial Rayleigh range determines the minimal depth resolution of the microscope. Alternatively, one can rely on temporal spreading of the beam, rather than spatial spreading, to produce the same intensity-dependent fluorescence effect. One can even perform scanningless depth-resolved multiphoton microscopy because a large beam can illuminate the entire sample in one shot, and the existence of temporal focus in each region of the beam removes the need for scanning [24]. Improvement of the contrast in line-scanning multiphoton microscopy has also been demonstrated [25, 26].

Coherent control using temporally focused pulses is possible by placing the system of interest within the temporal Rayleigh range of the beam. The temporal modulation of the beam is mapped onto different spatial positions in the sample, creating spatially dependent excitation conditions along the beam's propagation axis. Further pulse shaping using established techniques enables the application of arbitrary additional spectral phase functions to the pulse. We employ Fourier domain pulse shaping using a spatial light modulator (SLM) to precisely tailor the spectral phase of an input laser pulse. The SLM can be placed at the Fourier plane of the telescope in the spatio-temporal set-up or in a 4-f pulse shaping set-up earlier in the beam line [5]. The overall phase can be written as the sum of the conventional SLM spectral phase and the geometric z -dependent linear chirp:

$$\varphi_{\text{total}}(\omega, z) = \varphi_{\text{SLM}}(\omega) - 2\beta z\omega^2. \quad (2)$$

Using atomic caesium, we recently demonstrated that by combining pulse shaping with temporal focusing, the properties of the temporal focus can be altered by pulse shaping. For instance, the addition of a quadratic spectral phase changes the position of the temporal focus relative to the spatial focus, as anticipated from equations (1) and (2). Since TPA is maximized for a transform-limited pulse, i.e. a pulse with zero chirp, the physical position of a nonlinear process can be shifted along the propagation axis in a completely deterministic manner. By inducing a dark state using a π -step pulse [9], in addition to a quadratic spectral phase, a dark nonlinear focus is produced and can be deterministically shifted to a selected spatial region of the sample [27].

We note that spatio-temporal effects related to coherent control have been discussed in other scenarios. Two examples include propagation effects of laser pulses in resonant media [16] and the modulation of pulse shapes in high-gain laser amplifiers [28]. These well-established examples are 'passive' effects in the sense that the principle 'control' processes were the immutable properties of the medium. Little effort was put into taking advantage of these material properties by combining active pulse-shaping techniques with propagation effects. With the development of femtosecond pulse shaping over the past two decades, new approaches have been undertaken. Oron and Silberberg unified temporal focusing and pulse-shaping techniques in the context of improving depth resolution in multiphoton microscopy [29]. Dudovich *et al* examined the interplay between enhancement of coherent

transients and the propagation of shaped excitation pulses in strongly resonant media [30]. Nelson and colleagues have performed several studies using a different spatio-temporal control method, in which pulse trains are spatially multiplexed and individually shaped [31]. Each shaped pulse can then be directed to a chosen spot in the sample in order to create spatially dependent excitation conditions. Our spatio-temporal method allows us to measure the system response resulting from a simultaneous variation of two phase parameters, one of which is pulse chirp and the other being a spectral phase applied to a pulse shaper. Features of weak and strong field quantum control are intuitively visualized by mapping the data into two dimensions.

3. Theory: exploring symmetry properties of spatio-temporal plots

The weak field amplitude probability of the nonresonant two-photon absorption is given by [9]

$$a_f^{(nr)} \approx -\frac{1}{i\hbar^2} \sum_m \frac{\mu_{fm}\mu_{mg}}{w_{mg} - w_{fg}/2} \times \int_{-\infty}^{\infty} E(\omega_{fg}/2 + \omega)E(\omega_{fg}/2 - \omega) d\omega \quad (3)$$

where ω_{fg} is the transition frequency from the initial state $|g\rangle$ to the final state $|f\rangle$, the states $|m\rangle$ are far detuned intermediate states and the μ s represent transition dipole moments. For any antisymmetrical spectral phase around $\omega_{fg}/2$, the weak field two-photon transition probability is identical to that of the transform limited pulse. Thus, it was shown that when dealing with an arbitrary spectral phase, only the even part of the phase, $\varphi^{\text{even}}(\omega)$, governs the final excitation. We note that another symmetry relation affects TPA, namely that for any spectral phase profile $\varphi(\omega)$, the complementary spectral phase $-\varphi(\omega)$ will result in the same absolute value of the probability amplitude. This is easily seen by taking the complex conjugate of the expression in equation (3). These two symmetry properties can be formalized as discussed below.

In most temporal coherent control experiments, a *single* parameter is assigned to the spectral phase, such as a phase modulation or a phase shift. By choosing a phase parameter α that satisfies the antisymmetry relation $\varphi_{-\alpha}^{\text{even}}(\omega) = \text{const} - \varphi_{\alpha}^{\text{even}}(\omega)$ around $\omega_{fg}/2$, it is assured that for any value of α , there is a complimentary scanned value $-\alpha$ such that

$$|a_f^{(nr)}(\alpha; \omega_{fg}/2)| = |a_f^{(nr)}(-\alpha; \omega_{fg}/2)|. \quad (4)$$

Some commonly used scan parameters for which this is true include the very well-known π -step scan, where the parameter α is the location of the spectral π -step phase relative to the symmetry point $\omega_{fg}/2$. Here, $\varphi_{\alpha}^{\text{even}}(\omega; \omega_{fg}/2) = \frac{\pi}{4}[\text{sign}(\omega - \alpha) - \text{sign}(\omega + \alpha)]$, and it is easily shown that the anti-symmetry condition is satisfied. Thus a symmetric pattern with respect to α is expected [10]. Another simple example is the variation of a linear chirp parameter. In this case, the spectral phase satisfies $\varphi_{-\alpha}^{\text{even}}(\omega; \omega_{fg}/2) = -\alpha\omega^2 = -\varphi_{\alpha}^{\text{even}}(\omega; \omega_{fg}/2)$ and we again expect the amplitude probability to be symmetric as the parameter α is scanned.

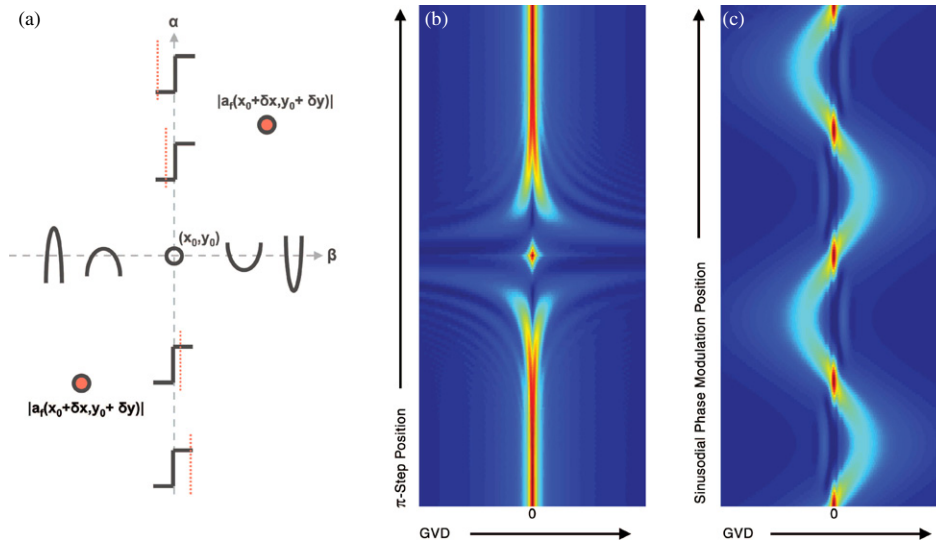


Figure 2. (a) 2D phase parameter map, each point represents the amplitude probability of a nonresonant two-photon absorption (TPA) as a function of two phase parameters: the pulse chirp and the π -step position relative to $\omega_{fg}/2$. The symmetry of the map is illustrated by equal amplitude probabilities of both points a_f in the sketch. TPA amplitude probability is calculated in (b), where the 2D map is symmetrical relative to a point obtained by a completely anti-symmetrical spectral phase. For the case of periodic phase parameters, such as a sinusoidal spectral phase modulation (c), more symmetry points are obtained.

This property can be generalized by writing $\varphi^{\text{even}}(\omega)$ as the sum of N independent phase parameters¹, i.e.

$$\varphi_{\alpha_1, \alpha_2, \dots, \alpha_N}^{\text{even}}(\omega; \omega_{\text{sym}}) \equiv \varphi_{\alpha_1}^{\text{even}}(\omega; \omega_{\text{sym}}) + \varphi_{\alpha_2}^{\text{even}}(\omega; \omega_{\text{sym}}) + \dots + \varphi_{\alpha_N}^{\text{even}}(\omega; \omega_{\text{sym}}). \quad (5)$$

It is then required that

$$\varphi_{-\alpha_1, -\alpha_2, \dots, -\alpha_N}^{\text{even}}(\omega; \omega_{\text{sym}}) = -\varphi_{\alpha_1, \alpha_2, \dots, \alpha_N}^{\text{even}}(\omega; \omega_{\text{sym}}), \quad (6)$$

to obtain the generalized expression:

$$|a_f^{(nr)}(\alpha_1, \alpha_2, \alpha_3, \dots, \alpha_N; \omega_{\text{sym}})| = |a_f^{(nr)}(-\alpha_1, -\alpha_2, -\alpha_3, \dots, -\alpha_N; \omega_{\text{sym}})|. \quad (7)$$

This shows that by applying a spectral phase that depends on parameters $\{\alpha_1, \alpha_2, \dots, \alpha_N\}$, the transition probability $|a_f^{(nr)}|$ is identical to that obtained using phase parameters $\{-\alpha_1, -\alpha_2, \dots, -\alpha_N\}$.

Using the spatio-temporal method, we control the spectral phase as per equation (2), which describes the summation of the spectral phase applied at the SLM and the linear chirp resulting from the temporal focusing of the pulse. This total phase has a similar structure as equation (5) for the case of two independent scan parameters, and by choosing an appropriate SLM phase such as those described as in the examples above, equation (6) is also satisfied. By mapping the data onto a two-dimensional grid, with axes corresponding to the two scanned parameters, the resulting plot will therefore be symmetric, as stated in equation (7). In figure 2, the vertical axis represents the parameter scanned using the SLM. The horizontal axis represents the linear chirp resulting from the pulse propagation. The amplitude probabilities of a

nonresonant TPA process are plotted in figures 2(b) and (c), for a π -step and a sinusoidal modulation scan, respectively. Note that by taking a slice along the vertical axis of figure 2(b), where the chirp equals zero, we recover the shape of the π -step scan obtained in [10] for nonresonant TPA in caesium. Similarly, along the vertical axis in figure 2(c), we recover the 1D sinusoidal modulation scan from [9]. There are obvious symmetries that appear in each of these 2D weak-field simulations. In the π -step example of figure 2(b), there is one symmetry point, which appears at the origin. For the sinusoidal modulation of figure 2(c), symmetry points appear periodically along the vertical axis, where the spectral phase is antisymmetric around $\omega_{fg}/2$.

In the non-perturbative regime however, the amplitude probability symmetry usually breaks down, as strong field effects such as Stark shifts, power broadenings and multiphoton ionization will occur. Nevertheless, there are special cases where the symmetry structure can be recovered. An elegant example for retaining the single phase parameter symmetry in strong fields was described recently using single quadrature fields [17]. In that study, the phase parameter was the modulation of a spectral sinusoidal phase function where real fields were obtained for antisymmetrical symmetrical phase envelope profiles around ω_{sym} . These fields lead to cancellation of power broadenings, and hence, points of equal probability amplitude are obtained in the same symmetrical fashion. The use of a complex-valued envelope field diminishes this symmetry and full Bloch sphere dynamics is needed. Two examples involving complex fields were investigated by Wollenhaupt *et al* and included the use of linear chirp and sinusoidally phased-modulated pulses [18, 19]. In order to describe the mechanism that breaks the symmetry we shall use a time domain approach that describes the strong field interaction with a two-level system, including dynamic Stark

¹ This is a sufficient, but not a necessary condition. The symmetry conditions hold as long as equation (6) is satisfied. A linear combination of independent phase parameters is the simplest functional form that will satisfy equation (6).

shifts, as described elsewhere [32–34]. The time-dependent Hamiltonian is obtained by performing adiabatic eliminations of all the other far detuned levels. Using the rotating wave approximation and moving to the rotating frame, the following Hamiltonian is obtained:

$$\hat{H}(t) = \begin{pmatrix} -\frac{1}{2} [\delta_\omega^{(s)}(t) + \Delta + \dot{\phi}(t)] & \chi^*(t) \\ \chi(t) & \frac{1}{2} [\delta_\omega^{(s)}(t) + \Delta + \dot{\phi}(t)] \end{pmatrix}, \quad (8)$$

where $\delta_\omega^{(s)} = \frac{1}{2} (\omega_e^{(s)}(t) - \omega_g^{(s)}(t))$ is the time-varying detuning, and $\omega_g^{(s)}(t), \omega_e^{(s)}(t)$ represent respectively the dynamic Stark shifts of the ground and excited states. $\chi(t)$ is the two-photon coupling field (or the two-photon time-varying Rabi frequency). All are given by the following summation on the far detuned levels [33, 35]:

$$\begin{aligned} \omega_g^{(s)}(t) &= - \sum_m \frac{\mu_{mg}^2 |\varepsilon(t)|^2}{2\hbar^2} \frac{\omega_{mg}}{\omega_{mg}^2 - \omega_0^2}, \\ \omega_e^{(s)}(t) &= - \sum_m \frac{\mu_{em}^2 |\varepsilon(t)|^2}{2\hbar^2} \frac{\omega_{em}}{\omega_{em}^2 - \omega_0^2}, \\ \chi(t) &= - \sum_m \frac{\mu_{em} \mu_{mg}}{4\hbar^2} \frac{\varepsilon^2(t)}{\omega_{mg} - \omega_0}. \end{aligned}$$

Trallero-Herrero *et al* [35] have shown that in order to achieve efficient population transfer of two-photon absorption, one should phase match the interaction, i.e. choose a phase which will cancel out the internal effective time-dependent detuning, caused by the dynamic Stark shift. It was also shown that the perturbative solution of this interaction [9] can be obtained from the general Hamiltonian in the limit that the ground state is not depleted, where $|a_g(t)| \simeq 1$, and the Stark shifts vanish, $\delta_\omega^{(s)} \approx 0$.

Each matrix component has a different dependence both on the dipole moment strengths and on the frequency intervals from the far detuned energy levels (note that the denominator of each matrix component is different). Since each component is furthermore dependent on the temporal envelope, the symmetry discussed earlier is no longer valid. In contrast to the weak-field regime, where spectral envelope asymmetry only scales the TPA rate, in the non-perturbative regime it affects dramatically the time domain envelope, and thus the population transfer. Additionally, the time-averaged effect of the dynamic Stark shift modifies the symmetry point location. The direction and the amount of the symmetry point movement will depend on the relative strength of the dipole moments, the detuning regarding the intermediate level and the field intensity.

Another complexity arises when an intermediate level is located near the spectral bandwidth. As the field intensity increases, the dynamic Stark shift will alter the effective energy structure of the levels, and may facilitate resonant transitions from that intermediate level. When dealing with resonant media, the symmetry condition is usually invalid, although there are cases where a specific phase parameter can retain the symmetry [17, 36]. Consequently, the influence of the linear chirp merits further elaboration because it is a special phase parameter that is fundamental for this work and

especially significant for resonant TPA processes. Previous studies have demonstrated how linear chirp can be used in population transfer schemes [12, 37, 38]. In these works three different pathways are discussed for transferring population from an initial state |1> to a final state |3>, in an unharmonic three-ladder system. The most intuitive path is accomplished when the instantaneous frequency of the laser pulse follows the spacing of the anharmonic ladder. Population transfer then occurs when the atom follows the fully adiabatic dressed potential curve. The second path describes a diabatic traversal of the ground-intermediate transition. For both these paths, the population of the upper state will be asymmetric in chirp, so that negative chirp will hardly cause any population transfer while positive chirp will efficiently populate the level. The final path deals with population that cannot be transferred via sequential absorption of single photons. Instead, transfer occurs via counterintuitive adiabatic crossing of the |3> \rightarrow |1> two-photon transition. If the middle, resonant level |2> is red detuned, it uses a scheme with a negatively chirped pulse. It is also necessary to use high intensities and slow frequency sweep, causing the system to adiabatically follow the eigenfunction of the coupled pulse-atom Hamiltonian.

4. Experimental set-up

Our experimental system, schematically plotted in figure 3(c), consists of a Ti:sapphire laser amplifier delivering 30 fs pulses at a repetition rate of 1 kHz (Femtolasers GmbH). The pulse-shaping apparatus uses a conventional 4-f configuration that contains 600 1/mm gratings, 10 cm parabolic mirror lenses and a programmable liquid crystal spatial light modulator (Jenoptics Phase SLM-640) placed in the Fourier plane. The SLM is used as a dynamic filter for spectral phase manipulation of the pulses. In the experiments, we used caesium atoms to realize the spatio-temporal interaction of shaped ultrashort pulses with a two-level system in the strong-field regime. caesium atoms were also used to compare resonant and nonresonant processes in two- and three-level systems in the weak-field regime. Last, rubidium atoms were used to realize the spatio-temporal interaction of unshaped ultrashort pulses with resonant two-photon absorption. In order to avoid an interaction with a fourth level, the laser spectrum (which had tails in the frequency of the $5P_{1/2}-5S_{1/2}$ transition at 795 nm) was cut using an amplitude mask. After the pulse shaper, the beam reflects off a 600 1/mm grating aligned perpendicular to the optical axis of a X10 telescope consisting of a 300 mm spherical lens and a 30 mm spherical achromat. These shaped, temporally dispersed pulses were then directed into caesium and rubidium cells that are maintained at a temperature of $\sim 70^\circ\text{C}$. The population of the effective ground state ($6S_{1/2}$ in caesium, $5S_{1/2}$ in rubidium) remains low enough at this elevated temperature to ensure that propagation effects due to resonant absorption will be negligible. In caesium, the excited state population was measured via fluorescent decay through the $7P$ level at 460 nm while for rubidium, fluorescence via the $6P_{1/2}$ level at 420 nm was detected. The fluorescence was

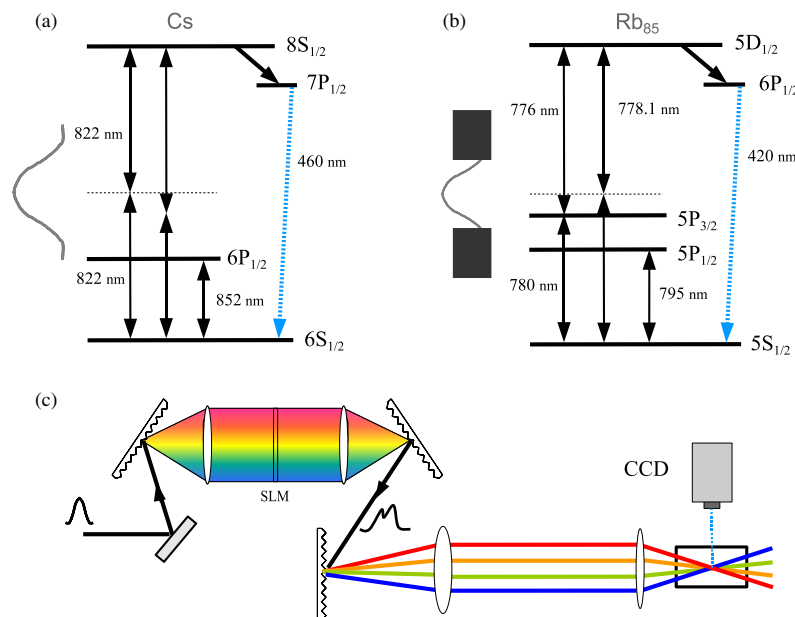


Figure 3. Energy level structure diagram for TPA processes in (a) atomic caesium $6S_{1/2} - 8S_{1/2}$ and (b) atomic $Rb_{85} 5S_{1/2} - 5P_{3/2} - 5D_{1/2}$. The excited state population is monitored via spontaneous decay fluorescence of each atom. In Rb_{85} , we blocked frequency components of the laser field to prevent it from exciting $5P_{1/2}$. (c) The experimental set-up, see text for further details.

imaged from above onto a CCD camera (Mintron MTV-12V1 CCIR) using a telescope with $M = \frac{5}{3}$.

As noted in section 2, we could have placed our SLM into the Fourier plane of the telescope in the temporal focusing set-up [27]. We chose to shape our pulses using a separate 4-f configuration in order to obtain better spectral resolution and to employ the appropriate strong field optics.

5. Results and discussion

Coherent control of multiphoton absorption in atomic caesium was investigated in order to observe the effects of increasing the excitation intensity into the strong-field regime. The results are summarized in a 2D map, shown in figure 4. A series of pulse shapes were produced by scanning a π -step spectral phase function across the pulse spectrum in 0.3 nm steps. For each spectral position of the π -step, a spatio-temporal image was recorded. Each image was integrated along the axis perpendicular to the propagation direction and was plotted on the horizontal axis as a function of its spatial position along the propagation axis. Equivalently, this axis represents the linear chirp applied to the pulse due to temporal focusing. The GVD was calculated to be $45 \text{ fs}^2 \mu\text{m}^{-1}$ using equation (1) and was confirmed by applying quadratic phase to the laser pulses using the SLM. The wavelength of the π -step applied to the SLM is plotted on the vertical axis. Spatio-temporal data were collected in this manner for five different intensities, spanning over one order of magnitude and covering the weak- and strong-field regimes.

Cross-sectioning the data along $z = 0$, the scans correspond to a 1D π -scan with unchirped pulses. Increasing the intensity leads to large enhancements of the multiphoton absorption signal compared to the weak-field excitation.

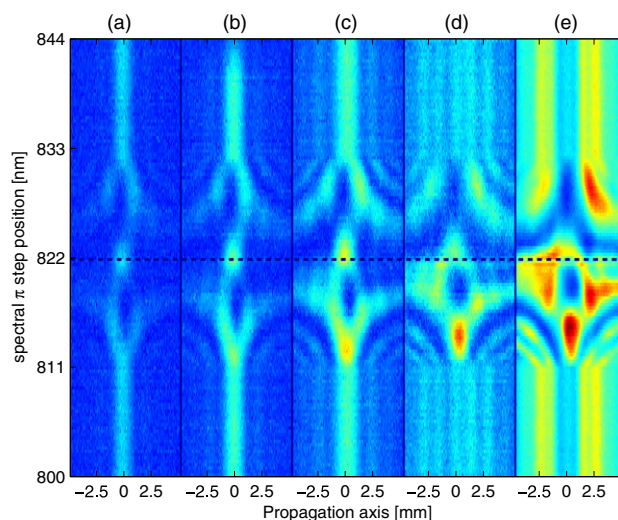


Figure 4. Spatio-temporal maps of the nonresonant TPA of atomic caesium at increasing field intensities (a) 1.9, (b) 4.1, (c) 6.6, (d) 11.6 and (e) 19.2 GW cm^{-2} . The scanned spectral phase parameter was the π step position relative to $\omega_{fg}/2$. For each π step position in each intensity, a spatio-temporal image was acquired. The horizontal axis describes the spatial coordinate along the propagation axis, whereas the vertical coordinate is the π -step position, as applied by the SLM. In relatively weak fields (a), (b), a symmetrical excitation pattern is clearly seen, as expected from the theoretical analysis. However, as intensity rises (c)–(e) the symmetry weakens, and the point of symmetry is shifted toward larger wavelength values.

This aspect of the data is in agreement with very recent work by other groups [35, 39]. However, the spatio-temporal plots reveal a great deal of information that is not

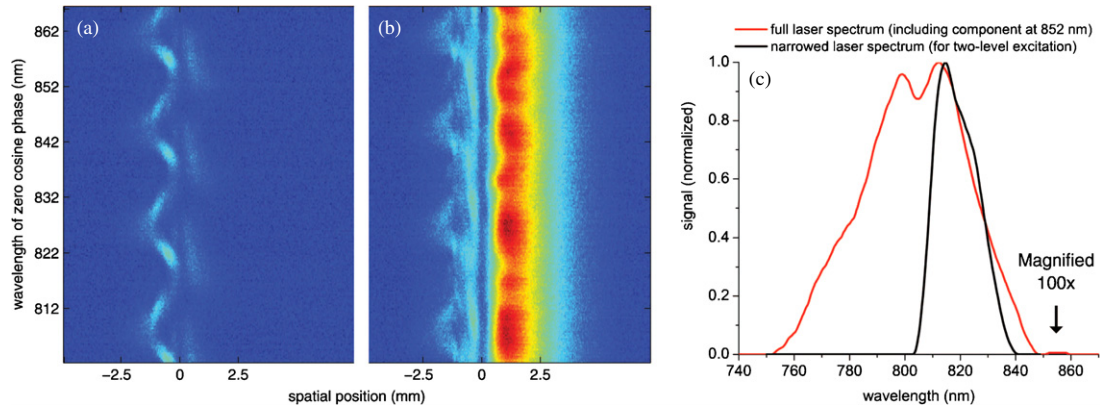


Figure 5. Separation of nonresonant and resonant TPA contributions by spatio-temporal maps. Here the phase parameter was a sinusoidal phase modulation generated by an SLM. The intensity at zero chirp is 1.4 GW cm^{-2} . (a) Narrowed laser spectrum addresses the non-resonant TPA process. The ‘phase imprinting’ effect is observed, and the periodicity of the phase parameter manifests in multiple symmetry points, as discussed earlier. (b) Full laser spectrum reveals resonant and non-resonant contributions of the TPA process. The spatio-temporal map allows us to visualize this separation. In both (a) and (b), an absence of TPA signal (ionization) is observed where the intensity reaches a maximum (see footnote 2). (c) The full and narrowed spectral envelopes used in the measurement.

accessible using purely temporal 1D methods. As discussed in section 3 and shown in figure 2, the spatio-temporal 2D plots show a symmetrical behaviour in the weak-field regime. The simulation in figure 2(b) compares favourably with the measured data from figure 4(a). There is a symmetry point (x_0, y_0) , where x_0 corresponds to the zero chirp value y_0 to the position of the antisymmetrical π -step phase at frequency $\omega_{fg}/2$. Relative to this symmetry point, each pixel has a counterpart pixel that satisfies the equation $|a_f(x_0 + \delta x, y_0 + \delta y)| = |a_f(x_0 - \delta x, y_0 - \delta y)|$. Upon increasing the field fluency, this symmetry is broken. In figure 4, we see the movement of the point (x_0, y_0) toward larger wavelengths, signifying a spectral shift toward the resonant level that relates to the magnitude of the dynamic Stark shifts of the ground and excited states. At the highest intensity that was measured (19.2 GW cm^{-2}), this shift is approximately 1.3 nm. There is additional reshaping of this feature as the intensity is increased. In the weak field, the peak centred on the symmetry point is symmetrical about both axes. With increasing intensity, it becomes elongated along the wavelength (vertical) axis, reflecting the broadening of the energy levels as determined by the time-averaged behaviour of the Stark shifting. A left–right asymmetrical structure is also observed, which is evidence of the influence of a third resonant level that becomes relevant due to the Stark shifting of the other two levels. The asymmetry can also arise due to an asymmetrical structure of the excitation spectrum, an effect that becomes significant in the strong-field regime. Further quantitative analysis of the symmetry properties in spatio-temporal plots will be forthcoming in a follow-up study [40].

Pathway information can be extracted in other ways using spatio-temporal control. By controlling the spectral content of excitation pulses, we have shown that resonant and nonresonant excitation pathways can be distinguished spatially. The interaction of shaped pulses with both two- and three-level systems in atomic caesium was analysed in the weak-field regime. When excited by a pulse whose spectrum is centred at 822 nm, caesium can be modelled as a two-level

system provided the bandwidth of the pulse is not large enough to include spectral components at 852 nm. A 20 nm bandwidth centred at 822 nm was chosen by using slits to block all other components in the Fourier plane at the SLM. Then, a sinusoidal spectral phase was applied to the pulse, as described by the equation $\varphi(\omega) = \gamma \cos(\tau\omega + \phi)$, where $\gamma = \frac{J_0^{(0)}}{2} = 1.205$ and $J_0^{(0)}$ is the first null value of the zeroth-order Bessel function J_0 . The spectral position of this sine phase was stepped across the laser spectrum, pixel by pixel, in 0.3 nm steps.

The most prominent feature in the data is the sinusoidal pattern along the vertical axis in figure 5. Near the $z = 0$ position, we recover the results of Meshulach and Silberberg for nonresonant TPA in caesium [9]. As per their analysis, the maximum fluorescence signal (maximum TPA rate) occurs when the sinusoidal function is antisymmetric around the centre of the excitation spectrum, with dark states (no TPA) occurring between the maxima. In the present study, we also observe how the two-photon signal is revived with the addition of a chirp component. The second derivative of the spectral phase function is equal to the total applied linear chirp, which, in the case of a temporally focused pulse, has a one-to-one correspondence with a position along the beam propagation axis. Thus, as expected based on the simulation in figure 2(c), we see the second derivative of the spectral phase imprinted along the vertical axis. This ‘phase imprinting’ property of our spatio-temporal technique is quite general when applied to nonresonant two-photon absorption processes in that any spectral phase function can be imprinted in the medium in this way. We also note the lack of fluorescence signal along $z = 0$, which is an indication of multiphoton ionization at this position (caused by a three-photon process in caesium), where the pulse reaches its maximum intensity². Also, a small initial positive chirp was present on the excitation pulses. This addition has

² The TPA maximum is observed at the temporal focus, where the pulse is transform limited; however, ionization occurs at the slightly shifted spatial focus where the excitation intensity is higher. This is an artefact due to the use of a cylindrical lens as one of the focusing optics.

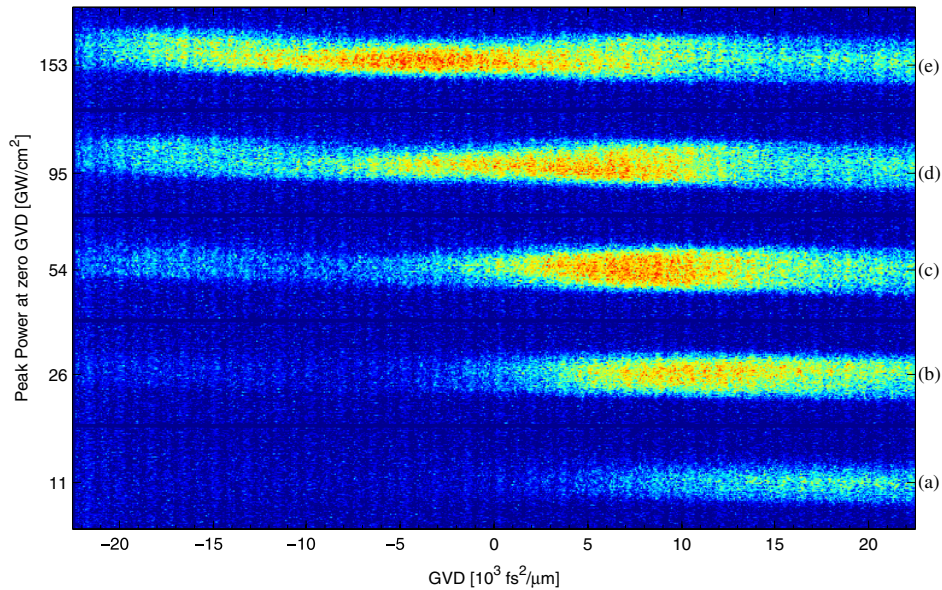


Figure 6. The transition from weak to strong field population control in three-level atomic Rb_{85} . For the following field intensities (a) 11, (b) 26, (c) 54, (d) 95 and (e) 153 GW cm^{-2} spatio-temporal CCD images were acquired. The propagation axis covers GVD values from $\{-2.25 \times 10^4 \text{ fs}^2 \mu\text{m}^{-1}$ to $2.25 \times 10^4 \text{ fs}^2 \mu\text{m}^{-1}\}$. In weak-to-intermediate field regimes, excitation occurs only for positive chirp values (right-hand side of the image), whereas for stronger intensities, the nonintuitive negative chirp contribution also becomes efficient.

no effect except for the shifting of the entire spatio-temporal excitation pattern through the negative z -direction [27].

By repeating the same scan with our full spectral envelope, i.e. by opening up the slits in the Fourier plane at the SLM to include the 852 nm contribution to the spectrum, we observed an extremely high two-photon absorption signal in the positive chirp regime of our measurements (right-hand side of the CCD image in figure 5(b)). This is due to sequential absorption of two one-photon processes, where a 852 nm photon is followed by one at 794 nm. Simultaneously, we observe the phase-imprinted nonresonant two-photon absorption pattern and the dark line signifying the presence of ionization. The intensity scale is identical in figures 5(a) and (b), so it is evident that the resonantly enhanced absorption process is more than twice as strong as the nonresonant one, even though the spectral power density at 852 nm is five orders of magnitude smaller than that at the peak of the pulse near 820 nm. The existence of this antisymmetrical behaviour of the resonant TPA in the weak-field regime was discussed by others [12, 37, 38]. For a three-level quantum system with a blue detuned resonant level, such as the case of sodium, the prominent signal would instead occur in the negative chirp region of the spatio-temporal plot. In those earlier studies, the interferences between the nonresonant two-photon absorption and the two sequential one-photon absorption were discussed, but their absolute values could not be separated and measured. The relative magnitude of both contributions renders it extremely difficult to isolate any one of them without completely suppressing the other using pulse-shaping methods. By spatially separating the contributions, the spatio-temporal method can simultaneously observe and quantify both resonant and nonresonant processes.

Weak-to-strong field control of population in three-level systems was also considered. Stimulated Raman adiabatic

passage (STIRAP) is a method of achieving full population transfer between selected energy levels [22, 41]. Instead of using time-delayed, monochromatic laser beams, the use of chirped pulses in the adiabatic regime can also lead to complete population transfer. We examined this process in atomic rubidium. Its energy level diagram is shown in figure 3(b). In the experiment, a transform limited, 30 fs excitation pulse was directed through the spatio-temporal set-up and into the rubidium gas sample cell. We took CCD images of the fluorescence at 420 nm at different excitation intensities. The results are shown in figure 6. Each CCD image covers the GVD range from $\{-2.25 \times 10^4 \text{ fs}^2 \mu\text{m}^{-1}, 2.25 \times 10^4 \text{ fs}^2 \mu\text{m}^{-1}\}$ along the propagation axis. The beam width in the medium was 0.3 mm, corresponding to 30 pixels in the y -direction. The estimated spatial overlap of the different frequencies (temporal Rayleigh range) is 8 mm, which corresponds to a temporal FWHM of $3.6 \times 10^4 \text{ fs}^2$. Outside these regions there is no overlap of different frequencies, and thus the excitation reduces tremendously. Clearly, we observed that in the weak-to-intermediate field regimes, excitation occurs only for positive chirp (right-hand side of the images). As the intensity is increased, the TPA process becomes efficient for the nonintuitive negative chirp.

Analysis of this process was described by Broers *et al* [37] and Maas *et al* [38], and was briefly explained in section 3. A comparison between our data and that published in [37, 38] reveals excellent agreement with their results³. However, the method presented here is much simpler because a complete set

³ The beating patterns observed at positive chirp by other groups were not observed here because the lowest intensity in our experiments corresponded to an intermediate regime intensity of 5 GW cm^{-2} . At these intensities, interference between the fully and partially adiabatic pathways is partially suppressed.

of measurements over a wide range of negative and positive chirp values can be recorded in one shot. There is no need for cumbersome chirp scans through scanning of compressor gratings or through phase modulation using a pulse-shaping apparatus. The chirp dependence is displayed along the propagation axis because pulses acquire positive linear chirp as they propagate in the spatio-temporal set-up.

6. Conclusion

Spatio-temporal coherent control in atomic caesium and rubidium was demonstrated in the weak and strong-field regimes. The resulting 2D plots reveal information that is not easily attained in purely 1D temporal methods. This is because spatio-temporal control is a multidimensional technique, in which it is possible to vary two pulse-shaping parameters simultaneously. One dimension is obtained by shaping the pulse using an SLM, and the other is scanned by a continuous chirping of the pulse using temporal focusing. In the weak-field regime, spatio-temporal plots can be characterized in a visually intuitive manner owing to their symmetrical properties. Breakdown of these symmetries as the field strength is increased contains information on these strong-field processes. Further quantification of the symmetry breaking is key for disentangling more complicated nonlinear processes in atomic and molecular systems. We believe that such two-dimensional presentations obtained through spatio-temporal control will provide a new tool for optimizing systems using fields with just a few control parameters.

Acknowledgments

The authors want to thank Dan Oron for several fruitful discussions. Financial support from the Israel Science Foundation and the Horowitz Foundation is gratefully acknowledged. BDB acknowledges the financial support of the Koshland Center for Basic Research. HS acknowledges the Azrieli Foundation for financial support.

References

- [1] Shapiro M and Brumer P 2003 *Principles of the Quantum Control of Molecular Processes* (New York: Wiley)
- [2] Dantus M and Lozovoy V V 2004 *Chem. Rev.* **104** 1813–59
- [3] Seideman T and Hamilton E 2005 *Advances in Atomic, Molecular and Optical Physics* vol 52 ed P Berman and C Lin (New York: Academic)
- [4] Weiner A M 2000 *Rev. Sci. Instrum.* **71** 1929–58
- [5] Wefers M M and Nelson K M 1995 *J. Opt. Soc. Am. B* **12** 1343–62
- [6] Verluise F, Laude V, Cheng Z, Spielmann C and Tournois P 2000 *Opt. Lett.* **25** 575–7
- [7] Judson R S and Rabitz H 1992 *Phys. Rev. Lett.* **68** 1500–3
- [8] Nuernberger P, Vogt G, Brixner T and Gerber G 2007 *Phys. Chem. Chem. Phys.* **9** 2470–97
- [9] Meshulach D and Silberberg Y 1998 *Nature* **396** 239–42
- [10] Meshulach D and Silberberg Y 1999 *Phys. Rev. A* **60** 1287–92
- [11] Dudovich N, Dayan B, Gallagher Faeder S M and Silberberg Y 2001 *Phys. Rev. Lett.* **86** 47–50
- [12] Chatel B, Degert J, Stock S and Girard B 2003 *Phys. Rev. A* **68** 041402–1–4
- [13] Chatel B, Degert J and Girard B 2004 *Phys. Rev. A* **70** 053414–1–10
- [14] Dai X, Lerch W E-B and Leone S R 2006 *Phys. Rev. A* **73** 023404–1–5
- [15] Citron M L, Gray H R, Gabel C W and Stroud C R Jr 1977 *Phys. Rev. A* **16** 1507–12
- [16] Allen L and Eberly J H 1975 *Optical Resonance and Two Level Systems* (New York: Dover)
- [17] Dudovich N, Polack T, Pe'er A and Silberberg Y 2005 *Phys. Rev. Lett.* **94** 083002–1–4
- [18] Wollenhaupt M, Prakelt A, Sarpe-Tudoran C, Liese D, Bayer T and Baumert T 2006 *Phys. Rev. A* **73** 063409–1–15
- [19] Wollenhaupt M, Prakelt A, Sarpe-Tudoran C, Liese D, Bayer T and Baumert T 2006 *J. Mod. Opt.* **52** 2187–95
- [20] Yatsenko L P, Romanenko V I, Shore B W, Halfmann T and Bergmann K 2005 *Phys. Rev. A* **71** 033418–1–10
- [21] Guérin S 1997 *Phys. Rev. A* **56** 1458–62
- [22] Bergmann K, Theuer H and Shore B W 1998 *Rev. Mod. Phys.* **70** 1003–25
- [23] Martinez O D 1987 *IEEE J. Quantum Electron.* **QE-23** 59–64
- [24] Oron D, Tal E and Silberberg Y 2005 *Opt. Exp.* **13** 1468–76
- [25] Tal E, Oron D and Silberberg Y 2005 *Opt. Lett.* **30** 1686–8
- [26] Zhu G, van Howe J, Durst M, Zipfel W and Xu C 2005 *Opt. Exp.* **13** 2153–9
- [27] Suchowski H, Oron D and Silberberg Y 2006 *Opt. Commun.* **264** 482–7
- [28] Frantz L M and Nodvik J S 1963 *J. Appl. Phys.* **34** 2346–9
- [29] Oron D and Silberberg Y 2005 *Opt. Exp.* **13** 9903–8
- [30] Dudovich N, Oron D and Silberberg Y 2002 *Phys. Rev. Lett.* **88** 123004–1–4
- [31] Feurer T, Vaughan J C and Nelson K A 2003 *Science* **299** 374–7
- [32] Grischkowsky D, Loy M M T and Liao P F 1975 *Phys. Rev. A* **12** 2514–33
- [33] Trallero-Herrero C, Cardoza D, Weinacht T C and Cohen J L 2005 *Phys. Rev. A* **71** 013423–1–6
- [34] Trallero-Herrero C, Cohen J L and Weinacht T C 2006 *Phys. Rev. Lett.* **96**
- [35] Trallero-Herrero C and Weinacht T C 2007 *Phys. Rev. A* **75** 063401–1–8
- [36] Panek P and Becker A 2006 *Phys. Rev. A* **74** 023408–1–6
- [37] Broers B, Van Linden van den Heuvell H B and Noordam L D 1992 *Phys. Rev. Lett.* **69** 2062–5
- [38] Maas D J, Rella C W, Antoine P, Toma E S and Noordam L D 1999 *Phys. Rev. A* **59** 1374–81
- [39] Chuntanov L, Rybak L, Gandmana A and Amitay Z 2007 unpublished
- [40] Suchowski H, Bruner B D, Natan A and Silberberg Y 2008 at press
- [41] Gaubatz U, Rudeki P, Schiemann S and Bergmann K 1990 *J. Chem. Phys.* **92** 5363–76